

Article

Efficient LED-Array Optical Wireless Power Transmission System for Portable Power Supply and Its Compact Modularization

Mingzhi Zhao  and Tomoyuki Miyamoto * 

Laboratory for Future Interdisciplinary Research of Science and Technology (FIRST), Institute of Innovative Research (IIR), Tokyo Institute of Technology, R2-39, 4259 Nagatsuta, Midori-ku, Yokohama 226-8503, Japan; zhao.m.ab@m.titech.ac.jp

* Correspondence: tmiyamot@pi.titech.ac.jp; Tel.: +81-45-924-5059

Abstract: Optical wireless power transmission (OWPT) has been a promising solution for remote power supply, eliminating the need for power cables or batteries. In this paper, we propose a light emitting diode (LED) array based OWPT system with improved transmission efficiency and compact system dimension. In this experiment, the proposed four-LED-array collimation scheme achieved a lens system efficiency as high as 70%, while obtaining an electrical power of 0.8 W from a $50 \times 50 \text{ mm}^2$ GaAs solar cell at 1 m. The emitting side with the lens system was integrated into a $120 \times 114 \times 61 \text{ mm}^3$ portable device by 3D printing. In addition, the thermal performance of the integrated module and the effective surface irradiance at the receiving side were analyzed in detail. The proposed system exhibits high efficiency and portability, with the advantageous potential to temporarily power remote devices.

Keywords: optical wireless power transmission; LED; GaAs solar cell; IoT; far-field WPT



Citation: Zhao, M.; Miyamoto, T. Efficient LED-Array Optical Wireless Power Transmission System for Portable Power Supply and Its Compact Modularization. *Photonics* **2023**, *10*, 824. <https://doi.org/10.3390/photonics10070824>

Received: 23 June 2023
Revised: 13 July 2023
Accepted: 13 July 2023
Published: 14 July 2023



Copyright: © 2023 by the authors. Licensee MDPI, Basel, Switzerland. This article is an open access article distributed under the terms and conditions of the Creative Commons Attribution (CC BY) license (<https://creativecommons.org/licenses/by/4.0/>).

1. Introduction

The growing demand for powering devices remotely has led to the development of various wireless power transmission (WPT) methods. Among these techniques, optical wireless power transmission (OWPT) has emerged as a promising technology and received notable attention in recent years [1]. Compared with the near-field WPT methods, such as electromagnetic induction and magnetic resonance [2], OWPT offers significant advantages, including long transmission distance and high directionality [3]. In addition, when compared with the microwave WPT of far-field methods, OWPT has a small configuration and long distance transmission with high beam collection ratio. Furthermore, OWPT does not suffer from the problem of electromagnetic interference (EMI) [4].

OWPT has a wide range of applications in various scenarios, including in space [5], under water [6,7], and with mobile objects [8,9], as well as the Internet of Things (IoT). The IoT involves connecting numerous and various devices to the Internet for remote monitoring and control [10]. OWPT provides a charging solution to enable IoT devices to operate in remote or mobile locations with fewer restrictions. It eliminates the need for a wired power source or battery replacement. Therefore, the development of a portable OWPT system for IoT terminals is highly attractive.

Recently, light emitting diodes (LEDs) have been considered a potential option for an OWPT power source. Some smart optical wireless link research related to LED light sources has been designed since 2012 [11,12]. LEDs have a long lifetime, low temperature dependence, and high emission efficiency [13]. Compared to laser diodes (LD), LEDs are considered the safer power source due to their low spatial coherence. The emission mechanism of LEDs is to generate incoherent light by spontaneous electron-hole recombination with a broad energy spectrum [14]. As a result, LEDs exhibit lower directionality and lower

power density compared to LDs. Although the maximum permissible exposure (MPE) regulation for LED products [15] cannot be solely determined by the power density, it is generally easier for LEDs to comply with the MPE regulation as a 1 W level power source with a suitable irradiation area [16]. In addition, LEDs operating at this low output level can configure a compact and lightweight heat sink design, allowing for easy integration into portable devices. The low temperature dependence of the device performance is effective in this compact configuration.

As for the research on LED-OWPT, the first high-performance system was reported by Zhou et al. in 2019, which achieved an electrical output of 200 mW from a 2.9 cm² solar cell at a distance of 1 m [17]. The power source with lenses was modularized into a portable device of 116 × 116 × 132 mm³. Subsequently, the output level was increased to 400 mW in 2021 [18]. Some research groups have explored the implementation of the LED-OWPT concept. Uchiyama et al. presented an LED-OWPT system which could power small electronic devices without batteries [19]. Wuthibenjaphonchai et al. demonstrated a wearable glucose sensor powered by an LED for diabetes-monitoring [20]. In 2022, the authors' group optimized the LED-OWPT output and obtained 500 mW from a 25 cm² GaAs solar cell at 1 m distance [21]. Recently, the highest output of 1 W was achieved from the same size solar cell [22]. However, the efficiency was not optimal and 65% of the optical power was lost during the transmission process. For the development of LED-OWPT, it will primarily focus on designing an efficient system and ensuring its applicability to a wide range of actual operating conditions.

In this research, we aim to propose an LED-OWPT system with improved efficiency. An OWPT system is specifically designed to be compact and portable, providing an efficient solution for a temporary power source. Section 2 outlines the efficiency factors of an OWPT system and evaluates the design of an LED collimation lens system. In Section 3, the simulation and experimental results illustrate the performance of the improved lens system. Additionally, it discusses the effective surface irradiation on the receiving side. In Section 4, the LEDs with the lens system are integrated as a portable device. And the thermal performance is measured and analyzed. Section 5 concludes the report.

2. Efficiency for Optical Wireless Power Transmission

2.1. Factors of OWPT System Efficiency

Efficiency is one of the most important factors of all wireless power transmission systems. In this section, OWPT efficiency is analyzed in elementary terms. Figure 1 shows a basic OWPT system, which is simplified as a light source, a lens system, and a light receiver (solar cell). Although the receiver does not receive sunlight, the term “solar cell” is used because the device operates on the same fundamental principle of photovoltaic conversion. From the perspective of the OWPT radiation, transmission, and irradiation process, the efficiencies of the entire systems are mainly divided into three parts: the emitting side efficiency, the lens system efficiency, and the receiving side efficiency.

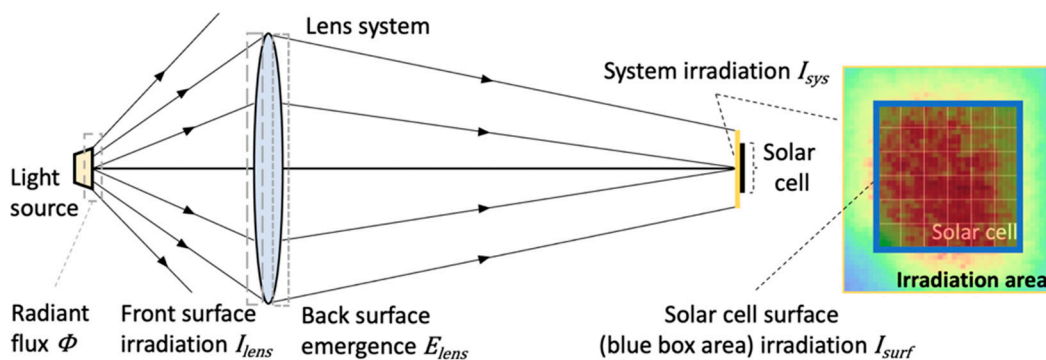


Figure 1. Simplified OWPT system for surface power and efficiency analysis.

Emitting side efficiency (η_{emit}) is the ratio of a power source’s radiant flux (Φ) to its electrical input power (P_{in}). It represents the electro-optical conversion ability of a power source.

$$\eta_{emit} = \frac{\Phi}{P_{in}} \tag{1}$$

Lens system efficiency (η_{lens}) is defined as the ratio of the total system irradiation power after a lens system (I_{sys}) to the radiant flux of the power source (Φ). It is used to evaluate the performance of the lens system in an OWPT, and is the main factor of this research.

$$\eta_{lens} = \frac{I_{sys}}{\Phi} \tag{2}$$

Receiving side efficiency (η_{recv}) is the product of the receiver photoelectric conversion efficiency (η_{PV}) and the effective surface irradiance (η_{surf}); η_{recv} quantifies the overall efficiency of the irradiation power at the receiving side into the electrical output. Here, η_{PV} also includes the effect of light intensity distribution within the solar cell module, while I_{surf} is the surface irradiation intensity at the solar cell surface and P_{out} is the electrical output from the solar cell.

$$\eta_{recv} = \eta_{surf} \times \eta_{PV} = \frac{I_{surf}}{I_{sys}} \times \frac{P_{out}}{I_{surf}} \tag{3}$$

As for the lens system efficiency, there are two factors: the transmissivity (T) and the divergence power rate (η_{div}). Lens transmissivity (T) is defined as the ratio of the emergent power from the lens system back surface (E_{lens}) to the irradiation power on the front surface (I_{lens}):

$$T = \frac{E_{lens}}{I_{lens}} \tag{4}$$

It is noted that the lens transmissivity does not include power absorption or scattering in the transmission medium. They are collectively considered in Equation (2). The divergence power in an OWPT emitting side is a part of the power source’s radiant power that is scattered out of the lens system area, thereby, the divergence power rate (η_{div}) is:

$$\eta_{div} = \frac{\Phi - I_{lens}}{\Phi} \tag{5}$$

These factors are used to evaluate the efficiency of an OWPT system. The symbols used in this research are listed in Table 1.

Table 1. Symbols for numerical analysis.

Notation	Description
Φ	Radiant flux of power source
I_{sys}	System total irradiation power
I_{surf}	Optical receiver surface irradiation power
I_{lens}	Irradiation power on lens system front surface
E_{lens}	Emergence power from lens system back surface
η_{surf}	Effective irradiance on receiver surface
η_{PV}	Photoelectric conversion efficiency of receiver
P_{in}	Electrical input power on power source
P_{out}	Electrical output power from receiver

2.2. Efficiency Evaluation of LED Collimation Scheme

In an OWPT system, the emitting side efficiency η_{emit} is determined by the semiconductor properties, material quality, and device structure of the power source [23]. Similarly, the photoelectric conversion efficiency η_{PV} of the receiver is also determined by the wavelength and the semiconductor bandgap [24]. The above two efficiencies are not analyzed in

this paper. Previous research by the authors’ group has proved that a combination of an 850 nm near-infrared light source and a flexible-type GaAs solar cell can achieve a high efficiency η_{PV} of 41.7% [17]. Even higher conversion efficiencies of 69% have been reported by the GaAs-based structure at an 858 nm wavelength, coupled with optimized beam irradiation conditions [25]. This research focuses on optimizing the lens system efficiency η_{lens} through non-imaging optics design.

We have proposed the LED collimation lens scheme [21], which consists of a collimation lens and an imaging lens. The configuration simulated by the optical simulation software (Zemax 2022, OpticStudio Premium, USA) is shown in Figure 2. The LED is placed at the front focal point of the collimation lens. Table 2 shows the parameters of the selected LED model [26]. The generated parallel beams are focused on the optical receiver by an imaging lens. The dimension of the effective emitting side depends on the lens aperture and the focal length of the collimation lens. According to the following analysis of the collimation scheme, this study will propose a more efficient lens system with a compact dimension.

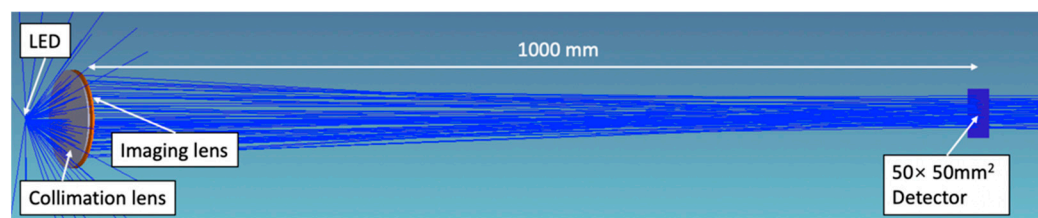


Figure 2. Simulated configuration of the LED collimation scheme.

Table 2. Parameter of the LED light source [26].

Model	OSRAM, SFH 4715AS
Wavelength	850 nm
FWHM	30 nm
Radiant flux	1.53 W
Divergence angle	$\pm 60^\circ$
Emitting panel area	$1 \times 1 \text{ mm}^2$

The efficiency of the LED collimation scheme is analyzed according to Section 2.1. In this scheme, the F-number of the collimation lens is found to be the only factor affecting the efficiency. The theoretical limit for the lens aperture in air is F-number = 0.5. In Figure 3a, the y-axis is the ratio of the surface power of different components to the LED radiant flux. The orange dashed curve with triangle marks represents the lens system efficiency (η_{lens}) according to Equation (2). Based on the front (black curve with square marks) and back surface power (blue curve with circle marks) of the lens system in Figure 3a, the transmissivity (T) and the divergence power rate (η_{div}) are calculated in Figure 3b according to Equations (4) and (5).

Figure 3a shows that the lens system efficiency increases as the F-number of the collimation lens decreases. This trend can be attributed to the $\pm 60^\circ$ LED divergence angle, which causes a large divergence power outside the lens surface range. In Figure 3b, the transmissivity of the lens system is relatively constant, ranging from approximately 80% to 95%. However, the F-number = 0.5 collimation lens has the smallest divergence power, indicating that it is the optimal choice for a high efficiency LED collimation scheme with minimal divergence. This means the diameter of the collimation lens should be twice its focal length.

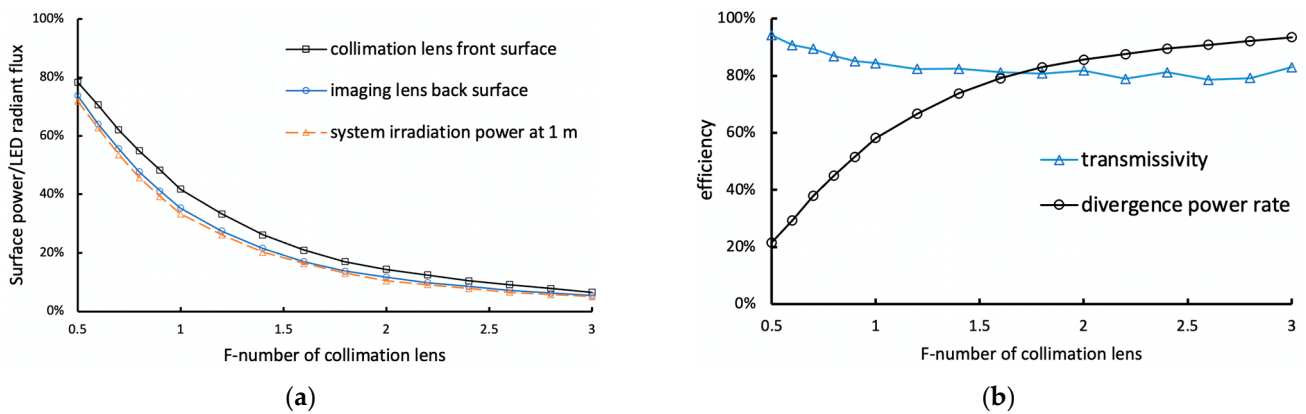


Figure 3. (a) Correlation between F-number of collimation lens and surface irradiation on various components; and (b) transmissivity and divergence power rate.

3. High Efficiency and Compact LED-OWPT System

3.1. Design and Experimental Setup

Due to the requirement of portability, the maximum lens aperture is limited to 100 mm by referring typical portable devices. Considering the dimensions of most IoT devices, the size of the solar cell is assumed to be up to $50 \times 50 \text{ mm}^2$. In addition, the initial ideal transmission distance is set to 1 m. According to the collimation scheme in Figure 2, LEDs and the corresponding collimation lens arrays are applied to improve the system output while maintaining a small irradiation area. As the size of the imaging lens is fixed, increasing the number of LEDs reduces the size of the collimator lens installed on each LED. As a result, there is a trade-off between the system efficiency and the total output. Figure 4 shows the simulated relationship between the solar cell surface irradiation (I_{surf}) and the effective solar cell surface irradiation (η_{surf}) as LED numbers change. As in the analysis in Section 2.2, all the collimation lenses satisfy the F-number = 0.5 in order to achieve the optimal efficiency of the lens system.

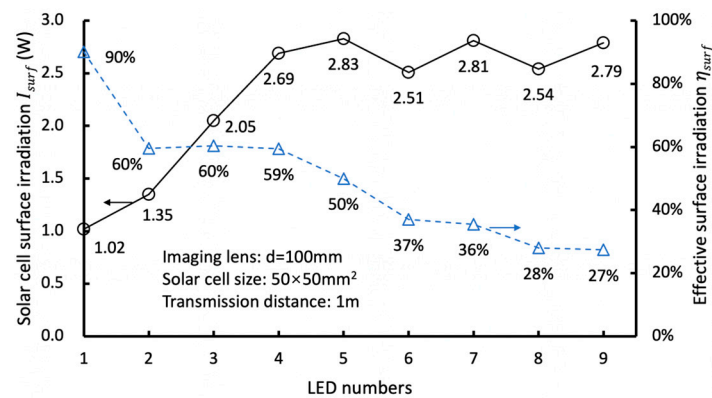


Figure 4. Simulated relationship between I_{surf} and η_{surf} as LED numbers varies. All the collimation lenses are fixed as F-number = 0.5.

In Figure 4, as the number of LEDs increases, although the lens system efficiency (η_{lens}) remains at the optimum, the size of the irradiation spot increases, resulting in a continuous decrease in effective solar cell surface irradiation (η_{surf}). In order to achieve both high efficiency and high output with less components for practical design, a four-LED-array collimation scheme with corresponding collimation lenses is applied. Figure 5 shows the proposed design in the Zemax simulation. The emitting side consists of four identical LEDs (OSRAM SFH4715AS; 850 nm, 1.53 W), arranged in a square shape array with a side length of 50 mm. By employing more LEDs in the optimal configuration, it is anticipated that the

output will be enhanced. However, the improvement over four-LED is relatively small, despite the need for a complex configuration with a large number of components.

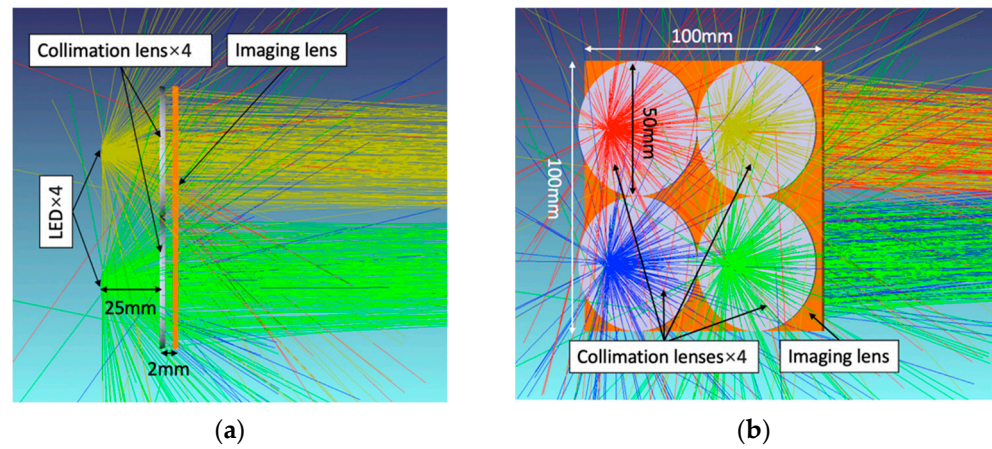


Figure 5. High efficiency LED-OWPT design: (a) view from side; and (b) view from LEDs.

The imaging lens is adapted to the aperture restrain ($a = 100 \times 100 \text{ mm}^2$, $f = 1000 \text{ mm}$). As in the analysis in Section 2.2, the same four collimation lenses ($d = 50 \text{ mm}$, $f = 25 \text{ mm}$) are placed at a distance of 25 mm away from the corresponding LEDs. The distance between the collimation lens and the imaging lens is set to 2 mm. To minimize the weight of the portable module, for a non-imaging system, Fresnel lenses made of plastic materials form the lens system. In addition, the Fresnel lens can be manufactured cost-effectively with F-number = 0.5 conditions. The expected performance will be analyzed in Section 3.2.

Figure 6 shows the experimental setup according to the simulation design. LEDs (OSRAM SFH4715AS) [26] with $d = 20 \text{ mm}$ submounts were screwed onto a $100 \times 100 \times 20 \text{ mm}^3$ aluminum heat sink. Four LEDs were connected in a series for flowing the same current to each LED and they were powered by a DC power source (MATSUSADA PRECISION, PK20-20). The applied voltage and current were 13.6 V and 1.5 A, respectively.

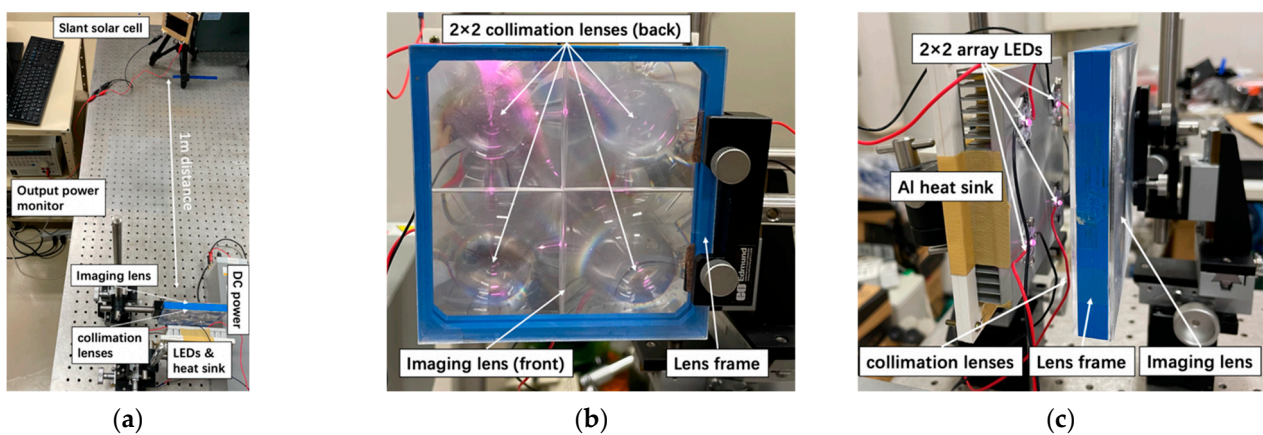


Figure 6. (a) Experiment setup; (b) front view of lens system; and (c) view from the LED side.

The lens system consists of four $f = 25 \text{ mm}$ Fresnel lenses (NTKJ, CF25) and one $f = 1000 \text{ mm}$ Fresnel lens (NTKJ, CF1000). For accurate assembly, square lens shapes are selected rather than circular shapes. The Fresnel patterns are formed up to the corners of a square. All the lenses are manufactured with anti-reflection (AR) coatings on both surfaces for NIR light. A 5-series connected GaAs solar cell with a total module size of $50 \times 85 \text{ mm}^2$ area is placed at 1000 mm from the imaging lens. The solar cell is rotated at an angle of 54° to the beam propagation direction, resulting in an effective surface irradiation area of $50 \times 50 \text{ mm}^2$.

The experiment was conducted under fluorescent lighting only. Although the GaAs solar cell also received a small amount of visible light from the fluorescent lamps, the solar cell output by the room light was evaluated as zero in the applied experimental setup.

3.2. Simulation and Experiment Results

The simulation results of the light intensity distribution are shown in Figure 7a–c. Figure 7a shows the system irradiation distribution at 1 m based on the incoherent light feature of the LED. The x -axis and y -axis describe the coordinate values of a $100 \times 100 \text{ mm}^2$ detector. In Figure 7b, the $50 \times 50 \text{ mm}^2$ solar cell surface irradiation power I_{surf} is 2.69 W. Figure 7c shows that the system irradiation power I_{sys} at 1 m is 4.41 W. The simulated irradiation spot area at 1 m is $67 \times 70 \text{ mm}^2$. From Equation (2), the lens system efficiency η_{lens} of the proposed design is 72.06%. Compared with the previous system $\eta_{lens} = 39.71\%$ [22], it is improved by 1.8 times.

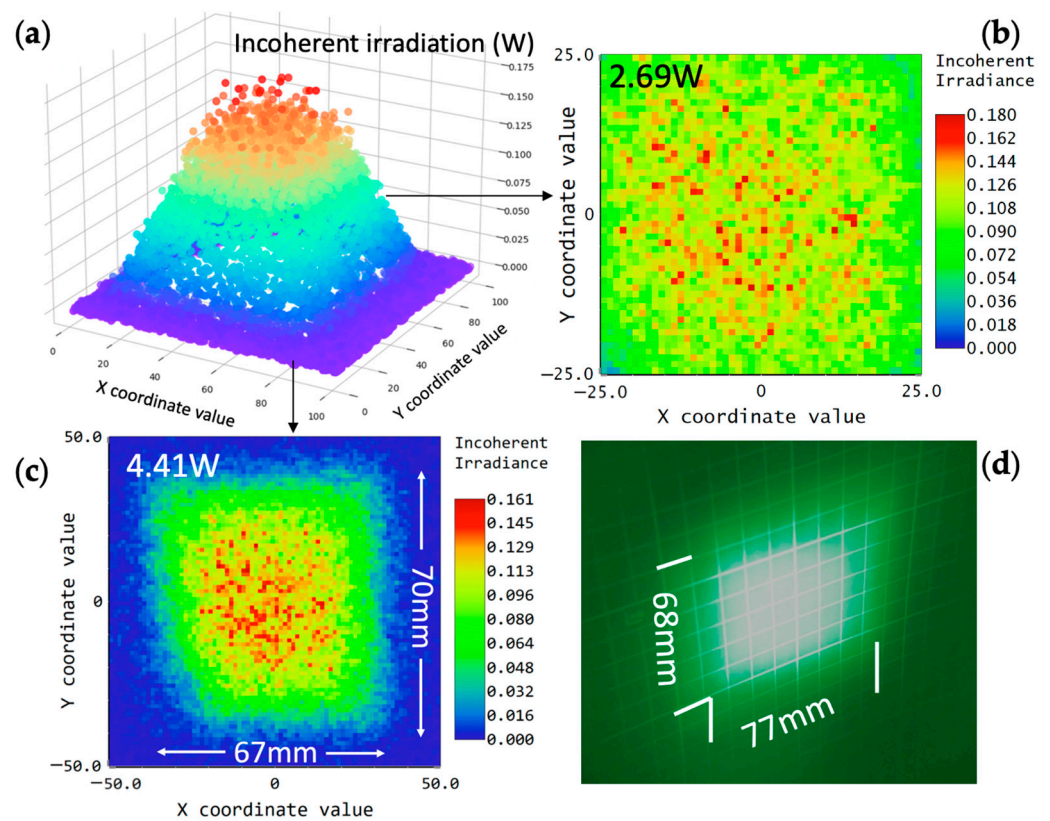


Figure 7. System performance at 1 m: (a) irradiation distribution; (b) $50 \times 50 \text{ mm}^2$ solar cell surface irradiation I_{surf} ; (c) total irradiation I_{sys} ; and (d) experiment observation by IR viewer.

In this experiment, as shown in Figure 7d, the irradiation spot area observed by an infrared viewer (ELECTROPHYSICS, ElectroViewer 7215) was $68 \times 77 \text{ mm}^2$. The grid board with a 10 mm scale grid was set perpendicular to the beam direction. The increased irradiation aberration was caused by the misalignment between the LEDs and the collimation lenses [27]. The electrical output was measured using an output monitor (ADCMT, 6243 DC Monitor). Figure 8 shows the current-voltage (I-V) and power-voltage (P-V) curves of the solar cell. As a result, the maximum power of the $50 \times 50 \text{ mm}^2$ effective area GaAs solar cell at 1 m was 0.795 W. The open circuit voltage and the short circuit current were 4.42 V and 0.29 A, respectively. The fill factor (FF) was 0.62.

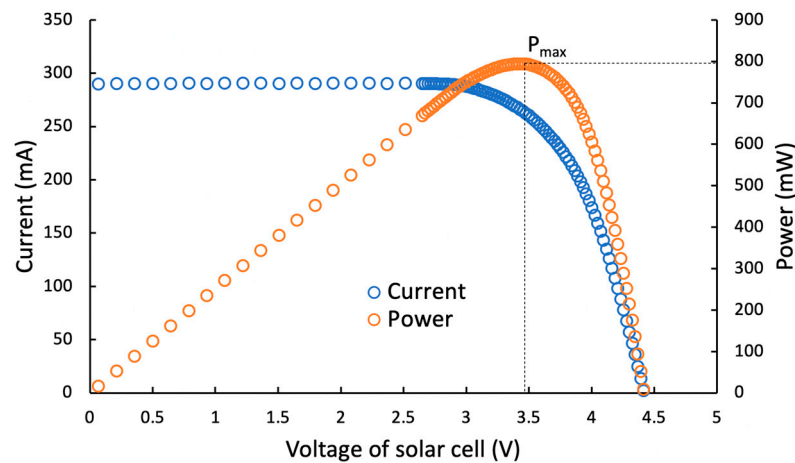


Figure 8. Current-voltage and power-voltage curves in this experiment.

According to the measurements by the power meter (COHERENT, FieldMax II), the $50 \times 50 \text{ mm}^2$ solar cell surface received 2.41 W of irradiation power. At a distance of 1 m, the system received a total irradiation of 4.29 W. The front and back surface irradiances of the lens system were 5.46 W and 4.75 W, respectively. Based on these measurements, the experimental efficiencies compared to the simulation values are shown in Table 3. The experimental results are consistent with the simulation results. In the case of indoor environment and air medium, the effects of absorption and scattering caused by the transmission medium can be considered negligible within a range of several meters.

Table 3. Simulation (sim.) and experiment (exp.) efficiency.

Efficiency	Sim. Result	Exp. Result
Emitting side efficiency (η_{emit})	N/A	30%
Lens system efficiency (η_{lens})	72.1%	70.1%
divergence power rate (η_{div})	9.2%	10.8%
Lens system transmissivity (T)	90.6%	87%
effective surface irradiation (η_{surf})	60.9%	56.2%

By applying the collimation lenses with F-number = 0.5, the beam leakage at the incident side can be effectively reduced. This modification to the lens system leads to a significant improvement in efficiency, which is approximately double that of the previous report [22]. Thus, the proposed LED-OWPT is regarded as a highly efficient design, and a promising candidate for practical applications.

3.3. Discussion of Effective Surface Irradiation

In the experimental setup of Section 3.1, the solar cell size is $50 \times 85 \text{ mm}^2$, which consists of five pieces of $50 \times 17 \text{ mm}^2$ GaAs cells in series. According to the dimension of most practical applications, this solar cell size is set as $50 \times 50 \text{ mm}^2$ along the optical path by the oblique setting. From the analysis of Equation (3), increasing the solar cell size or decreasing the irradiation spot size can improve the system output. Here, we will discuss the effective surface irradiation (η_{surf}) on the receiving side.

For a single-chip solar cell, whether it is a single-junction or multi-junction, the system irradiation area can be minimized. The ideal irradiation spot can be much smaller than the solar cell itself. However, in the case of a series-connected solar cell, it is necessary to ensure that the irradiation area covers each cell in the series. Otherwise, the output of the solar cell will be close to zero, because some pieces of the cells outside the irradiation area are not conductive [28].

Figure 9a shows the simulated incoherent irradiation power at 1 m using the single LED collimation configuration in Figure 2. The x and y axes represent the coordinates of an

80 × 80 mm² detector, while the z-axis represents the irradiation power corresponding to each coordinate. For a square shaped solar cell, the side length is assumed to range from 0 to 80 mm at a distance of 1 m. Figure 9b shows the solar cell surface irradiation, where the x-axis is the ratio of the side length of the solar cell to the system irradiation area, and the y-axis is the effective surface irradiation (η_{surf}).

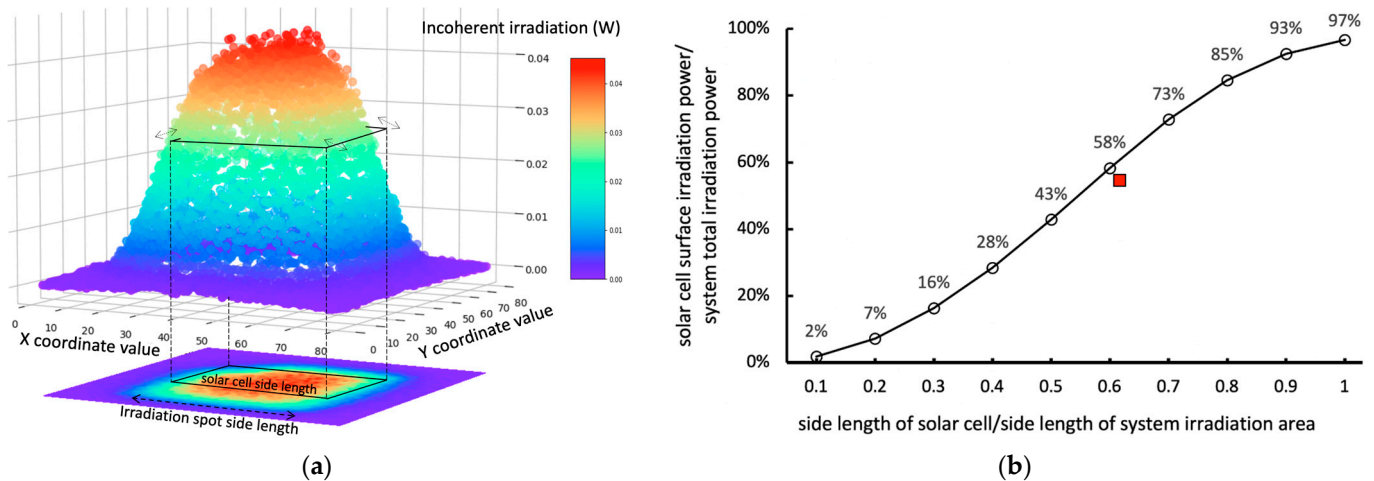


Figure 9. Effective surface irradiation: (a) system irradiation at 1 m; and (b) simulation result. The square red mark represents the experimental result by the configuration in Section 3.1.

The simulation results show that the effective surface irradiation strongly depends on the side length ratio between the irradiant spot and the solar cell. The relationship between the effective surface irradiation and the side length ratio is close to direct proportion. The edge irradiance of 1/10 of the center peak is considered the spot border. When the assumed receiver size is the same as this, there are still a few stray lights out of range, leading to a result of 97%. For illustration, the square red mark shows the experimental situation in Section 3.1. When the side length of the solar cell is extended to 80 mm (1.6 times larger than in this experiment), the effective surface irradiation (η_{surf}) is around 94%.

These results provide a scheme for optimizing the OWPT receiving side, particularly in terms of determining the appropriate size of the irradiation area relative to the solar cell size.

4. Integrated Module for Portable Power Supply

4.1. Demonstration of Portable Power Source Module

In Figure 6, the light source system was installed on the optical stage. In this section, we integrate the emitting side, consisting of a heat sink, LEDs, and lenses, into a portable module. This integration is shown in Figure 10. In principle, the optical characteristics and optical wireless power supply characteristics of this module are the same as those in Section 3. However, because it is susceptible to equipment manufacturing errors, detailed power supply characteristics will be optimized and evaluated in the future. Other practical features of compact modularization are discussed here.

The arrangement is the same as the design shown in Figure 5. The box frame was designed using a 3D modeling software (SketchUp Pro; Trimble Ltd. USA) and was fabricated using an LCD-based stereolithography 3D printer (Flashforge Foto 8.9 s) with Photopolymer resin material. This integrated device has a relatively small dimension and light weight. Figure 10b shows that the overall dimensions are 120 × 114 × 61 mm³. The heat sink with four LEDs weighs 233.4 g, and the weight of all the Fresnel lenses is 56.8 g. The total weight of the integrated light power source device is 407.1 g. The dimensions and weight are confined within an acceptable range, comparable to those of relatively large flashlights. Figure 10c shows the back and side holes for fin cooling. Due to its compact

size and light weight, this power source can be conveniently carried by humans or robots for temporary power supply.

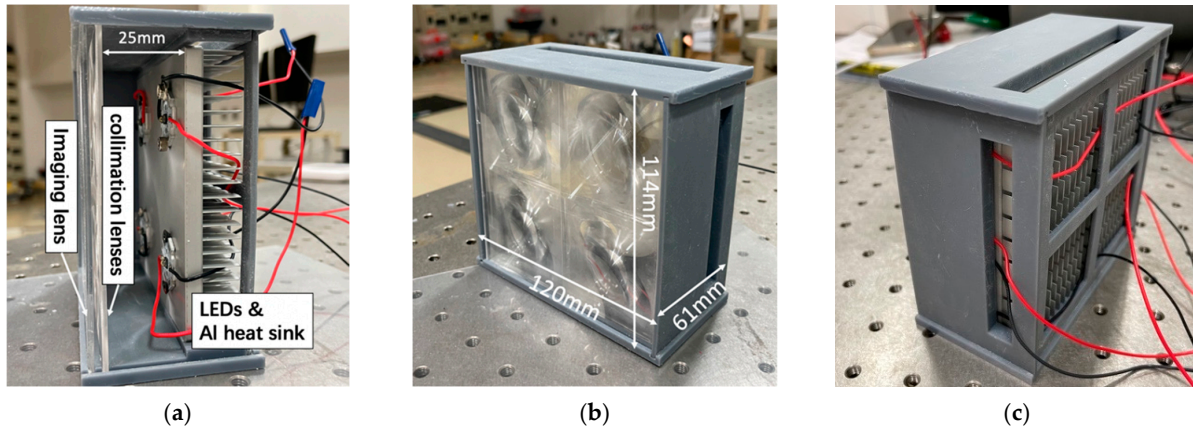


Figure 10. Portable power source module; (a) internal; (b) dimension; and (c) back.

4.2. Thermal Performance of Portable Power Source Module

The injected electrical power of an LED is not only converted into light energy but also results in some heat loss. In general, the electro-light conversion efficiency η_{emit} of a high power LED is about 15–40% [29,30]. In the case of the proposed light source module, the injected electric power P_{in} was 20.4 W, and the total radiant flux Φ of four-LEDs was measured as 6.12 W. The electro-light conversion efficiency η_{emit} was 30% for the experimental setup. As a result, about 14.3 W of heat was generated based on the above values.

For the portable module, the thermal performance was measured using a thermal shot camera (Avio Infrared Ltd., F30W). The integrated system was operated for 30 min under constant ambient temperature of 24 °C with the airflow of the room air conditioner. No fans were directed towards to the heat sink. Figure 11 shows the thermal images and the temperatures at the position of the cross mark. In the integrated module, the temperature distribution was non-uniform, where the LED chip performed the highest temperatures, reaching up to 68.5 °C. Figure 11a shows that the temperature of the aluminum heat sink ($237 \text{ W}\cdot\text{m}^{-1}\text{K}^{-1}$) [31] was 45.2 °C. Although the thermal conductivity of the resin frame limited the heat dissipation, the temperature of the resin frame surface ($0.5 \text{ W}\cdot\text{m}^{-1}\text{K}^{-1}$) [32] was about 25–35 °C, as shown in Figure 11b,c. The highest temperature that occurred closest to the LED was recorded as 36.3 °C.

For this integrated module, the aluminum heat sink and the heat dissipation holes are sufficient for thermal design. The surface temperatures remain within acceptable limits as a portable device, and it does not cause the attenuation of LED radiation. For further thermal optimization, some customized cooling systems need to be considered, such as higher performance heat sink designs or additional small fans.

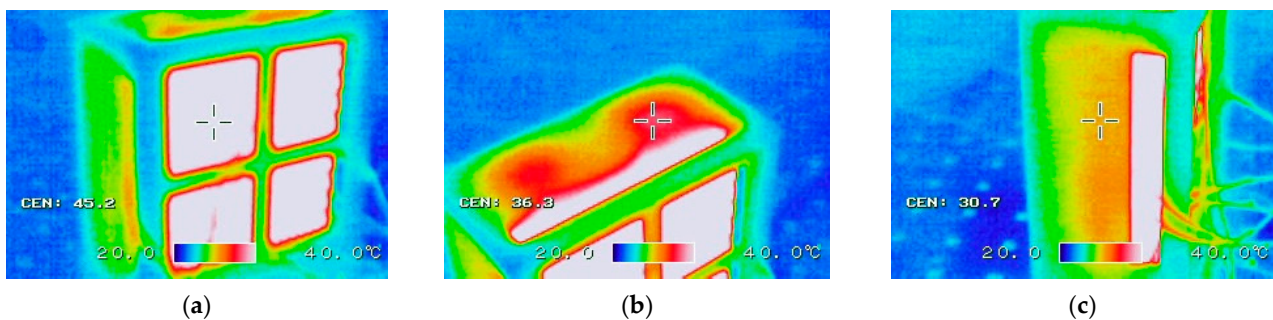


Figure 11. Thermal image and center temperature: (a) aluminum heat sink; (b) frame upper surface; and (c) side surface.

5. Conclusions

In this research, the proposed LED-OWPT provides a potential solution for improving the efficiency and portability of wireless power transmission systems. In this experiment, 70% lens system efficiency is achieved by the four-LED-array collimation scheme. The experimental result also shows 0.8 W electrical output from the $50 \times 50 \text{ mm}^2$ GaAs solar cell at 1 m transmission distance. The emitting side is integrated into a portable module with a compact dimension of $120 \times 114 \times 61 \text{ mm}^3$ and a weight of 407 g. In addition, the thermal performances have been tested, and the results prove the feasibility of the integrated configuration as a practical power source. The effective surface irradiation is discussed according to the relationship between the irradiation area and the solar cell size.

Overall, the LED-OWPT in this research provides a promising method with high efficiency and portability. The system has the potential to power IoT terminals for temporary and remote supplements. Some practical functions will be extended in further research.

Author Contributions: Conceptualization and methodology, M.Z. and T.M.; Software, experiment, validation, and data curation, M.Z.; Formal analysis, T.M.; Writing original draft preparation, M.Z.; Writing review and editing, T.M.; Supervision, administration, and funding acquisition, T.M. All authors have read and agreed to the published version of the manuscript.

Funding: This research was funded by Tsurugi-Photonics Foundation (No. 20220502), Takahashi Industrial and Economic Research Foundation (No. I2-003-13) and JST SPRING (JPMJSP2106).

Institutional Review Board Statement: Not applicable.

Informed Consent Statement: Not applicable.

Conflicts of Interest: The authors declare no conflict of interest.

References

1. Jin, K.; Zhou, W. Wireless Laser Power Transmission: A Review of Recent Progress. *IEEE Trans. Power Electron.* **2019**, *34*, 3842–3859. [[CrossRef](#)]
2. Jawad, A.M.; Nordin, R.; Gharghan, S.K.; Jawad, H.M.; Ismail, M. Opportunities and Challenges for Near-Field Wireless Power Transfer: A Review. *Energies* **2017**, *10*, 1022. [[CrossRef](#)]
3. Cheah, W.C.; Watson, S.A.; Lennox, B. Limitations of Wireless Power Transfer Technologies for Mobile Robots. *Wirel. Power Transf.* **2019**, *6*, 175–189. [[CrossRef](#)]
4. Miyamoto, T. Optical Wireless Power Transmission Using VCSELs. In *Semiconductor Lasers and Laser Dynamics VIII*; SPIE: Bellingham, WA, USA, 2018; Volume 10682, p. 1068204. [[CrossRef](#)]
5. Qaraqe, M.; Usman, M.; Serbes, A.; Ansari, I.S.; Alouini, M.-S. Power Hotspots in Space: Powering CubeSats via Inter-Satellite Optical Wireless Power Transfer. *IEEE Internet Things Mag.* **2022**, *5*, 180–185. [[CrossRef](#)]
6. Setiawan Putra, A.W.; Tanizawa, M.; Maruyama, T. Optical Wireless Power Transmission Using Si Photovoltaic through Air, Water, and Skin. *IEEE Photonics Technol. Lett.* **2019**, *31*, 157–160. [[CrossRef](#)]
7. Tai, Y.; Miyamoto, T. Experimental Characterization of High Tolerance to Beam Irradiation Conditions of Light Beam Power Receiving Module for Optical Wireless Power Transmission Equipped with a Fly-Eye Lens System. *Energies* **2022**, *15*, 7388. [[CrossRef](#)]
8. Nguyen, D.H. Optical Wireless Power Transfer for Moving Objects as A Life-Support Technology. In Proceedings of the 2020 IEEE 2nd Global Conference on Life Sciences and Technologies (LifeTech), Kyoto, Japan, 10–12 March 2020; pp. 405–408. [[CrossRef](#)]
9. Shindo, N.; Kobatake, T.; Masson, D.; Fafard, S.; Matsuura, M. Optically Powered and Controlled Drones Using Optical Fibers for Airborne Base Stations. *Photonics* **2022**, *9*, 882. [[CrossRef](#)]
10. Malche, T.; Maheshwary, P. Internet of Things (IoT) for Building Smart Home System. In Proceedings of the 2017 International Conference on I-SMAC (IoT in Social, Mobile, Analytics and Cloud) (I-SMAC), Palladam, India, 10–11 February 2017; pp. 65–70. [[CrossRef](#)]
11. Riza, N.A.; Murracini, P.J. Power Smart In-Door Optical Wireless Link Applications. In Proceedings of the 2012 8th International Wireless Communications and Mobile Computing Conference (IWCMC), Limassol, Cyprus, 27–31 August 2012; pp. 327–332. [[CrossRef](#)]
12. Murracini, P.J.; Riza, N.A. Smart Multiple-Mode Indoor Optical Wireless Design and Multimode Light Source Smart Energy-Efficient Links. *Opt. Eng.* **2013**, *52*, 055001. [[CrossRef](#)]
13. Jeon, S.O.; Lee, K.H.; Kim, J.S.; Ihn, S.-G.; Chung, Y.S.; Kim, J.W.; Lee, H.; Kim, S.; Choi, H.; Lee, J.Y. High-Efficiency, Long-Lifetime Deep-Blue Organic Light-Emitting Diodes. *Nat. Photonics* **2021**, *15*, 208–215. [[CrossRef](#)]
14. Piprek, J. Energy Efficiency Analysis of GaN-Based Blue Light Emitters. *ECS J. Solid State Sci. Technol.* **2019**, *9*, 015008. [[CrossRef](#)]

15. IEC 62471:2006 | IEC Webstore. Available online: <https://webstore.iec.ch/publication/7076> (accessed on 4 May 2023).
16. Rizzo, L.; Duncan, K.J.; Zunino, J.L.; Federici, J.F. Direct Beam Hazard Analysis of Large Beam Diameters for Laser Power Beaming. *J. Laser Appl.* **2018**, *30*, 032017. [[CrossRef](#)]
17. Zhou, Y.; Miyamoto, T. 200 MW-Class LED-Based Optical Wireless Power Transmission for Compact IoT. *Jpn. J. Appl. Phys.* **2019**, *58*, SJJC04. [[CrossRef](#)]
18. Zhou, Y.; Miyamoto, T. 400 MW Class High Output Power from LED-Array Optical Wireless Power Transmission System for Compact IoT. *IEICE Electron. Express* **2021**, *18*, 20200405. [[CrossRef](#)]
19. Uchiyama, N.; Yamada, H. Proposal and Demonstration of LED Optical Wireless Power-Transmission Systems for Battery-Operated Small Electronic Devices. *Jpn. J. Appl. Phys.* **2020**, *59*, 124501. [[CrossRef](#)]
20. Wuthibenjaphonchai, N.; Haruta, M.; Sasagawa, K.; Tokuda, T.; Carrara, S.; Ohta, J. Wearable and Battery-Free Health-Monitoring Devices with Optical Power Transfer. *IEEE Sens. J.* **2021**, *21*, 9402–9412. [[CrossRef](#)]
21. Zhao, M.; Miyamoto, T. Optimization for Compact and High Output LED-Based Optical Wireless Power Transmission System. *Photonics* **2022**, *9*, 14. [[CrossRef](#)]
22. Zhao, M.; Miyamoto, T. 1 W High Performance LED-Array Based Optical Wireless Power Transmission System for IoT Terminals. *Photonics* **2022**, *9*, 576. [[CrossRef](#)]
23. Saeedifard, M.; Graovac, M.; Dias, R.F.; Iravani, R. DC Power Systems: Challenges and Opportunities. In Proceedings of the IEEE PES General Meeting, Minneapolis, MN, USA, 25–29 July 2010; pp. 1–7. [[CrossRef](#)]
24. Florescu, M.; Lee, H.; Puscasu, I.; Pralle, M.; Florescu, L.; Ting, D.Z.; Dowling, J.P. Improving Solar Cell Efficiency Using Photonic Band-Gap Materials. *Sol. Energy Mater. Sol. Cells* **2007**, *91*, 1599–1610. [[CrossRef](#)]
25. Helmers, H.; Lopez, E.; Höhn, O.; Lackner, D.; Schön, J.; Schauerte, M.; Schachtner, M.; Dimroth, F.; Bett, A.W. 68.9% Efficient GaAs-Based Photonic Power Conversion Enabled by Photon Recycling and Optical Resonance. *Phys. Status Solidi (RRL)—Rapid Res. Lett.* **2021**, *15*, 2100113. [[CrossRef](#)]
26. OSRAM OSOLON®Black, SFH 4715AS IR LEDs—Ams-Osram. Available online: <https://ams-osram.com/products/leds/ir-leds/osram-oslon-black-sfh-4715as> (accessed on 4 May 2023).
27. Zhou, Y.; Miyamoto, T. Tolerant Distance and Alignment Deviation Analysis of LED-Based Portable Optical Wireless Power Transmission System for Compact IoT. *IEEJ Trans. Electron. Inf. Syst.* **2021**, *141*, 1274–1280. [[CrossRef](#)]
28. Tang, J.; Matsunaga, K.; Miyamoto, T. Numerical Analysis of Power Generation Characteristics in Beam Irradiation Control of Indoor OWPT System. *Opt. Rev.* **2020**, *27*, 170–176. [[CrossRef](#)]
29. Ben Abdelmek, K.; Araoud, Z.; Ghnay, R.; Abderrazak, K.; Charrada, K.; Zisis, G. Effect of Thermal Conduction Path Deficiency on Thermal Properties of LEDs Package. *Appl. Therm. Eng.* **2016**, *102*, 251–260. [[CrossRef](#)]
30. Wang, N.; Gao, C.; Ding, C.; Jia, H.-Z.; Sui, G.-R.; Gao, X.-M. A Thermal Management System to Reuse Thermal Waste Released by High-Power Light-Emitting Diodes. *IEEE Trans. Electron. Devices* **2019**, *66*, 4790–4797. [[CrossRef](#)]
31. Thermal Properties: Material Thermal Properties Database. Available online: https://ncfs.ucf.edu/burn_db/Thermal_Properties/material_thermal.html (accessed on 4 May 2023).
32. Guo, Y.; Ruan, K.; Shi, X.; Yang, X.; Gu, J. Factors Affecting Thermal Conductivities of the Polymers and Polymer Composites: A Review. *Compos. Sci. Technol.* **2020**, *193*, 108134. [[CrossRef](#)]

Disclaimer/Publisher’s Note: The statements, opinions and data contained in all publications are solely those of the individual author(s) and contributor(s) and not of MDPI and/or the editor(s). MDPI and/or the editor(s) disclaim responsibility for any injury to people or property resulting from any ideas, methods, instructions or products referred to in the content.